SUPPORTING INFORMATION

Effects of Electrochemical Conditioning on Nickel-Based Oxygen Evolution Electrocatalysts

Yoon Jun Son,[†] Seonwoo Kim,[†] Vanessa Leung,[†] Kenta Kawashima,[††] Jungchul Noh,[†]
Kihoon Kim,[†] Raul A. Marquez,[††] Omar A. Carrasco-Jaim,[†] Lettie A. Smith,[††]
Hugo Celio,[‡] Delia J. Milliron,[†,††] Brian A. Korgel,[†,‡] C. Buddie Mullins*[,†,††,‡,‡‡,§]

[†] McKetta Department of Chemical Engineering, [††] Department of Chemistry, [‡] Texas Materials Institute, [‡‡] Center for Electrochemistry, and [§] H2@UT, The University of Texas at Austin, Austin, Texas 78712, United States

Corresponding author.

---

*E-mail: mullins@che.utexas.edu

Table S1. Summary of experimental samples sorted according to the type of material (*i.e.*, Ni and NiSe), substrate (*i.e.*, FTO glass and Ni foil), electrochemical (EC) conditioning method (*i.e.*, CP, CA, and CV), and electrolyte (*i.e.*, Fe-purified and Fe-unpurified 1 M KOH).

	Substrate	EC conditioning	Electrolyte
1. Ni-initial	N/A	N/A	Fe-purified
2. Ni-CP	N/A	CP	Fe-purified
3. Ni-CV	N/A	CV	Fe-purified
4. Ni-initial	N/A	N/A	Fe-unpurified
5. Ni-CP	N/A	CP	Fe-unpurified
6. Ni-CV	N/A	CV	Fe-unpurified
7. Ni-CP$_1$-CP$_2$	N/A	1. CP 2. CP	1.Fe-purified 2. Fe-unpurified
8. Ni-CV$_1$-CP$_2$	N/A	1. CV 2. CP	1. Fe-purified 2. Fe-unpurified
9. Ni-CP-R	N/A	1. CP 2. CA	1. Fe-unpurified 2. Fe-unpurified
10. Ni-CV-R	N/A	1. CV 2. CA	1. Fe-unpurified 2. Fe-unpurified
11. 100-NiSe/FTO-CP	FTO	CP	Fe-purified
12. 200-NiSe/FTO-CP	FTO	CP	Fe-purified
13. 300-NiSe/FTO-CP	FTO	CP	Fe-purified
14. 100-NiSe/FTO-CV	FTO	CV	Fe-purified
15. 200-NiSe/FTO-CV	FTO	CV	Fe-purified
16. 300-NiSe/FTO-CV	FTO	CV	Fe-purified
17. 100-NiSe/Ni-CP	Ni foil	CP	Fe-purified
18. 100-NiSe/Ni-CV	Ni foil	CV	Fe-purified
19. 100-NiSe/Ni-CP	Ni foil	CP	Fe-unpurified
20. 100-NiSe/Ni-CP	Ni foil	CV	Fe-unpurified

Table S2. Concentrations (in ppb) of Fe ions in Fe-purified and Fe-unpurified 1 M KOH electrolyte obtained through solution mode ICP-MS.

	^{56}Fe [ppb]	Average Fe [ppb]	Standard Deviation	Standard Error
Fe-purified 1 M KOH 1	9.98	10.1	2.6	1.5
Fe-purified 1 M KOH 2	12.8			
Fe-purified 1 M KOH 3	7.58			
Fe-unpurified 1 M KOH 1	68.1	66.3	2.6	1.8
Fe-unpurified 1 M KOH 2	64.4			

ICP-MS analyses were performed to examine the molar concentration of Fe ions in Fe-purified and Fe-unpurified 1 M KOH electrolytes. As displayed in **Table S2**, Fe-unpurified 1 M KOH electrolyte contains 66.3 ppb of Fe ions, whereas Fe-purified 1 M KOH electrolyte contains 10.1 ppb of Fe ions. This result indicates that the Fe-purification process can effectively decrease the content of Fe impurities in KOH electrolyte, but not perfectly. According to the previous study by Chung *et al.*, the Fe content of the electrolyte can affect the rates of Fe dissolution and redeposition over a MO_xH_y host, determining the dynamically stable Fe composition incorporated into MO_xH_y.[1] In this regard, it is understood that the rate of Fe dissolution was faster than that of Fe (re)deposition for our experiments in Fe-purified 1 M KOH electrolyte, resulting in no (or negligible) Fe-incorporation into NiO_xH_y layer; OER activity enhancement or redox peak shift by Fe incorporation was not observed at all in our electrochemical data conducted in Fe-purified 1 M KOH electrolyte.

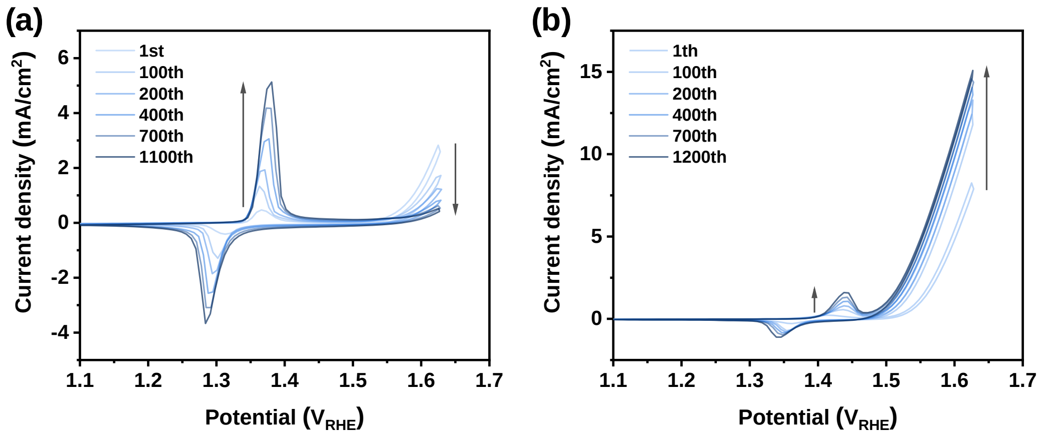

Figure S1. Electrochemical conditioning of Ni foil using CV at a scan rate of 20 mV/s in (a) Fe-purified and (b) Fe-unpurified 1 M KOH electrolytes.

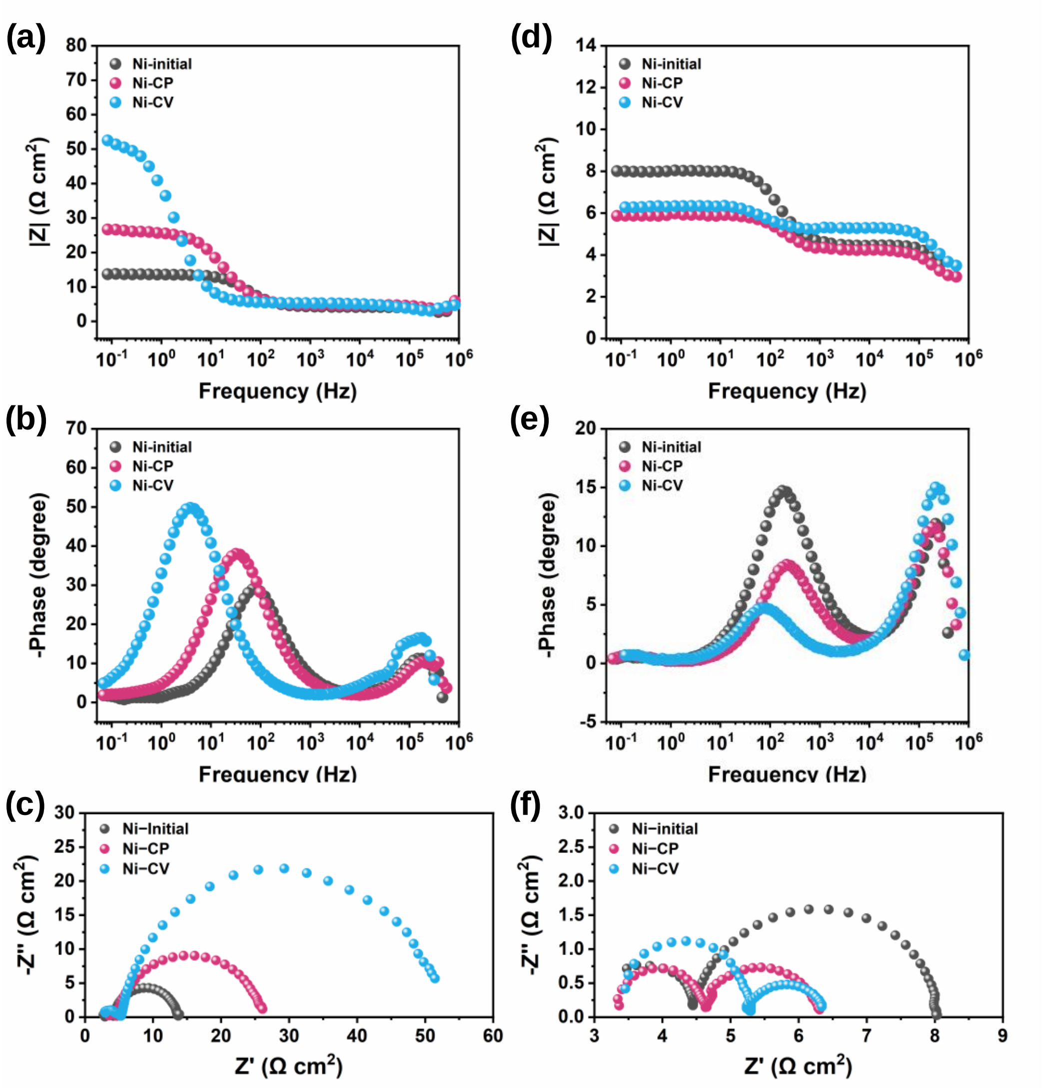

Figure S2. EIS spectra of Ni-initial, Ni-CP and Ni-CV measured at 1.63 V_{RHE} in (a-c) Fe-purified and (d-f) Fe-unpurified 1 M KOH electrolytes. (a,b,d,e) Bode plots, (c,f) Nyquist plots.

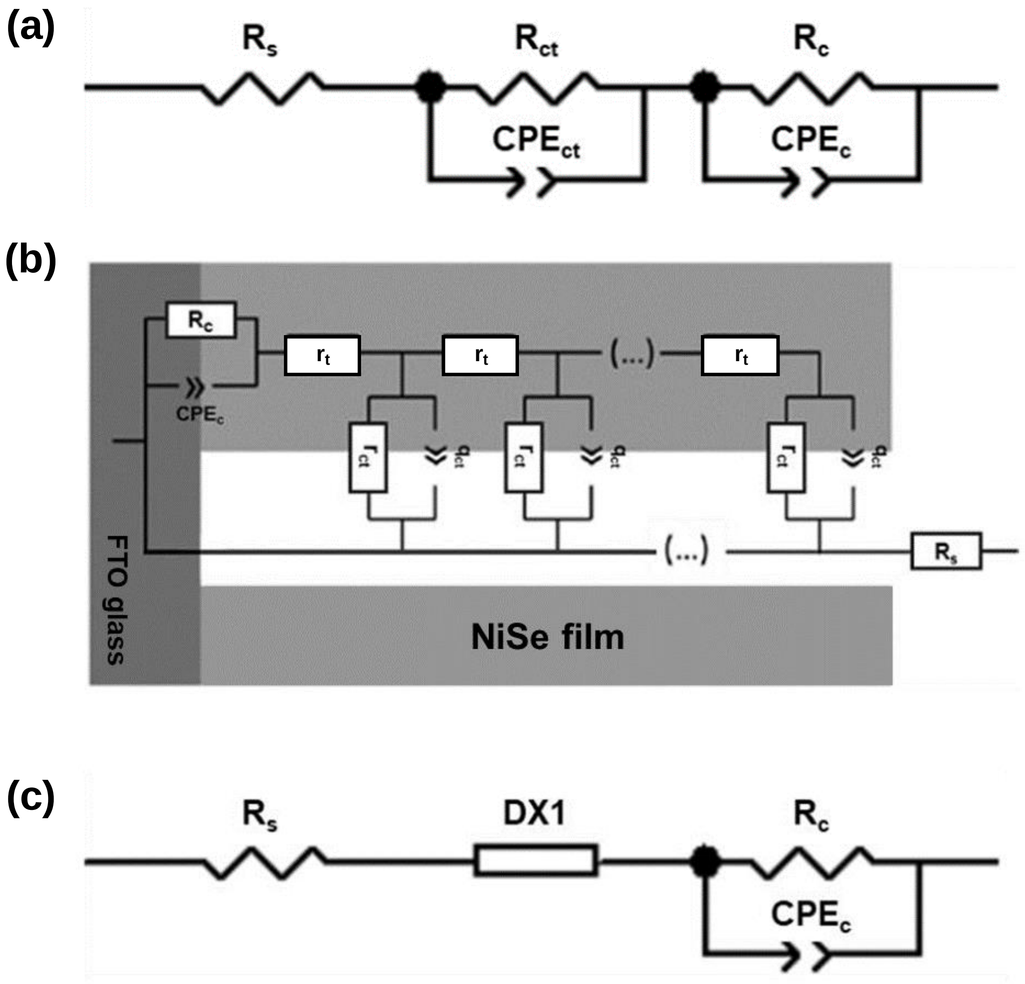

Figure S3. Equivalent circuit models for EIS data fitting. (a) Randle circuit for Ni-initial, Ni-CP, and Ni-CV, (b) Transmission line model for porous materials,[2] and (c) Equivalent circuit in Zview software for transmission line model.

In **Figure S2c,f**, Nyquist plots of the EIS spectra for Ni-initial, Ni-CP, and Ni-CV samples consist of two semicircles. The semicircle at higher frequencies is related to the contact impedance between the working electrode and the titanium clip that connects the working electrode to the potentiostats. The other semicircle at lower frequencies is related to the electrochemical phenomena at the interface between the electrocatalyst and electrolyte.

In **Figure S3**, R_s is a series resistance from solution resistance of electrolyte. R_c [Ω] and CPE_c [S sec^n] represent an impedance originating from the contact between the working electrode (catalyst electrode such as Ni foil, NiSe/FTO, and NiSe/Ni samples) and titanium clip. R_{ct} [Ω] is total charge transfer resistance at the whole catalytic interface and CPE_{ct} [S sec^n] is the constant phase element reflecting the whole catalytic interface. In **Figure S3b**, the r_t, r_{ct}, and q_{ct} represent distributed transport resistance, distributed charge transfer resistance, and distributed constant phase element through the porous structure in the transmission line model, respectively, and obey the following expressions,[3]

$$R_t = r_t \times L$$

$$R_{ct} = R_{ct} / L$$

$$CPE_{ct} = q_{ct} \times L$$

where R_t [Ω] is transport resistance related to electron and mass transport across the whole catalyst layer and L represents the thickness of the porous oxide layer.

Figure S3c shows the equivalent circuit model in Zview software with the extended element "Bisquert #2", which is "DX1-type 11" model for actual EIS fitting of the transmission line model in **Figure S3b**.[2,4] The double layer capacitance (C_{dl}) [F] was calculated according to the following equation,

$$C_{dl} = CPE_{ct} \times (w_{max})^{n-1}$$

where w_{max} [sec^{-1}] is the frequency at which the imaginary component reaches a maximum, n represents the degree of depression of the semicircle compared with an ideal semicircle and has a value less than 1.0.

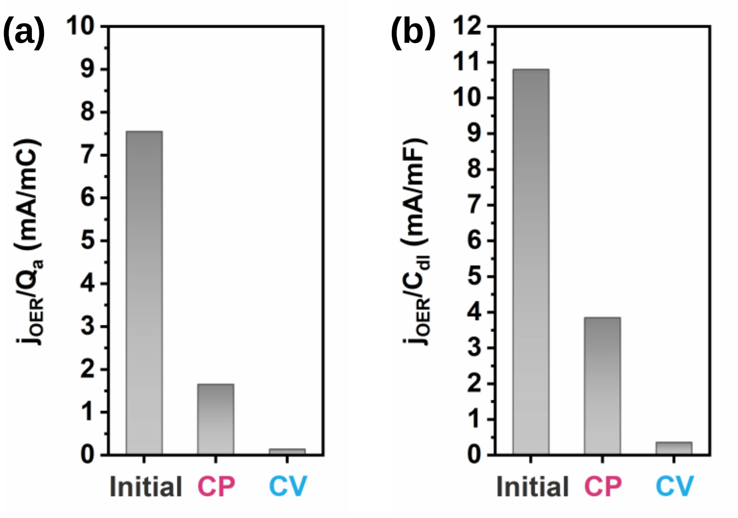

Figure S4. Electrochemical analyses of Ni foil before and after CP and CV electrochemical conditioning in Fe-purified 1 M KOH electrolyte. (a) j_{OER}/Q_a and (b) j_{OER}/C_{dl}. Here, Q_a, C_{dl}, and j_{OER} in **Figure 1b-d** were employed.

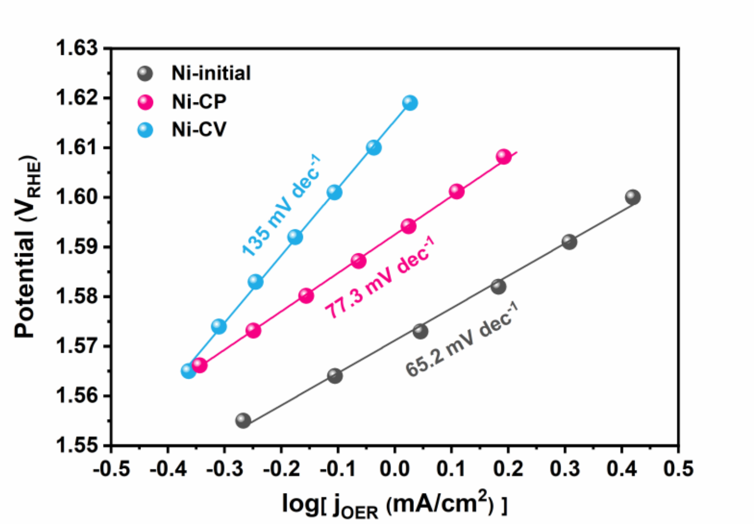

Figure S5. Tafel slopes of Ni-initial, Ni-CP, and Ni-CV in Fe-purified 1 M KOH.

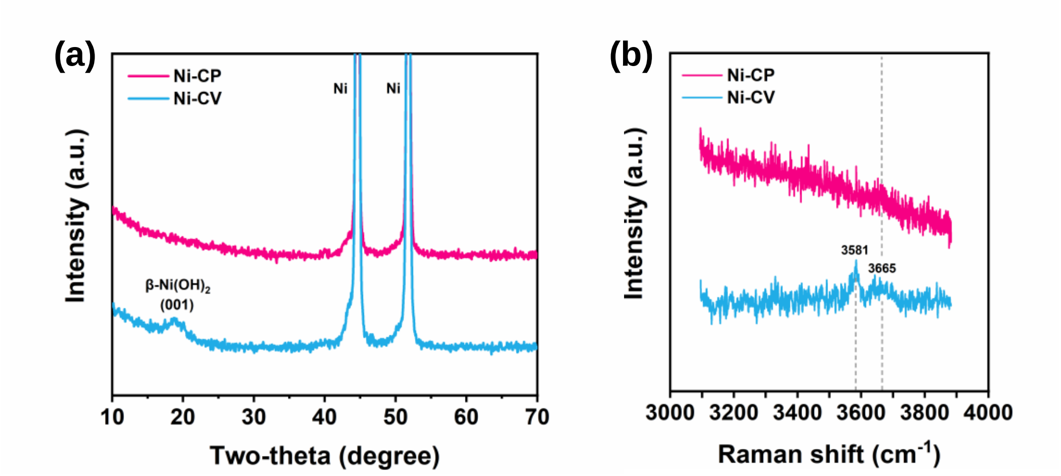

Figure S6. (a) GIXRD and (b) Raman spectra of Ni foil after CP and CV in Fe-purified 1 M KOH.

Grazing incidence X-ray diffraction (GIXRD) analyses for Ni-CP and Ni-CV were performed to examine the crystal structure of the very thin film (*i.e.*, NiO_xH_y layer on Ni foil), which is usually not detected using normal XRD analysis because weak signals from thin films are buried by strong background signals of substrates. As shown in **Figure S6a,** except for two metallic Ni peaks from the underlying Ni foil at two-theta degrees of 44.5° and 51.8°, Ni-CV showed a peak at 19.9° corresponding to the (001) plane of β-$Ni(OH)_2$ but no characteristic peak for α-$Ni(OH)_2$ probably due to the relatively weak signal of amorphous α-$Ni(OH)_2$.[5,6] On the other hand, Ni-CP did not exhibit any peak for α- and β-$Ni(OH)_2$ due to its too thin NiO_xH_y layer; to obtain the discernible GIXRD signals, Trotochaud et al. employed 150-200 nm thick α- and β-$Ni(OH)_2$ films, which would be much thicker than NiO_xH_y layer of Ni-CP and Ni-CV.[5]

To better characterize the crystal phase of α- and β-$Ni(OH)_2$, Raman spectra for Ni-CP and Ni-CV were acquired in the O−H stretching region at wavenumber (3100-3900 cm^{-1}), which represents O−H stretching bands of the lattice OH groups in $Ni(OH)_2$.[7] β-$Ni(OH)_2$ has a characteristic O−H stretch at around 3581 cm^{-1} whereas α-$Ni(OH)_2$ contains a broad, weak O−H stretch band centered at ~3575 cm^{-1}.[8,9] **Figure S6b** shows that Ni-CV has O−H stretching bands at 3581 and 3665 cm^{-1}, which are consistent with β- and α-$Ni(OH)_2$, respectively. On the other hand, Ni-CP does not have any peak at around 3581 cm^{-1} for β- $Ni(OH)_2$, but has the feature at around 3665 cm^{-1} for α-$Ni(OH)_2$, which is very weak due to the low signal-to-noise ratio of O-H stretching bands of α-$Ni(OH)_2$ and a thinner thickness of NiO_xH_y of Ni-CP compared to Ni-CV.

Thus, based on GIXRD and Raman spectra analyses, it is concluded that Ni-CV has a mixture of α- and β-$Ni(OH)_2$ whereas Ni-CP consists of mainly α-$Ni(OH)_2$.

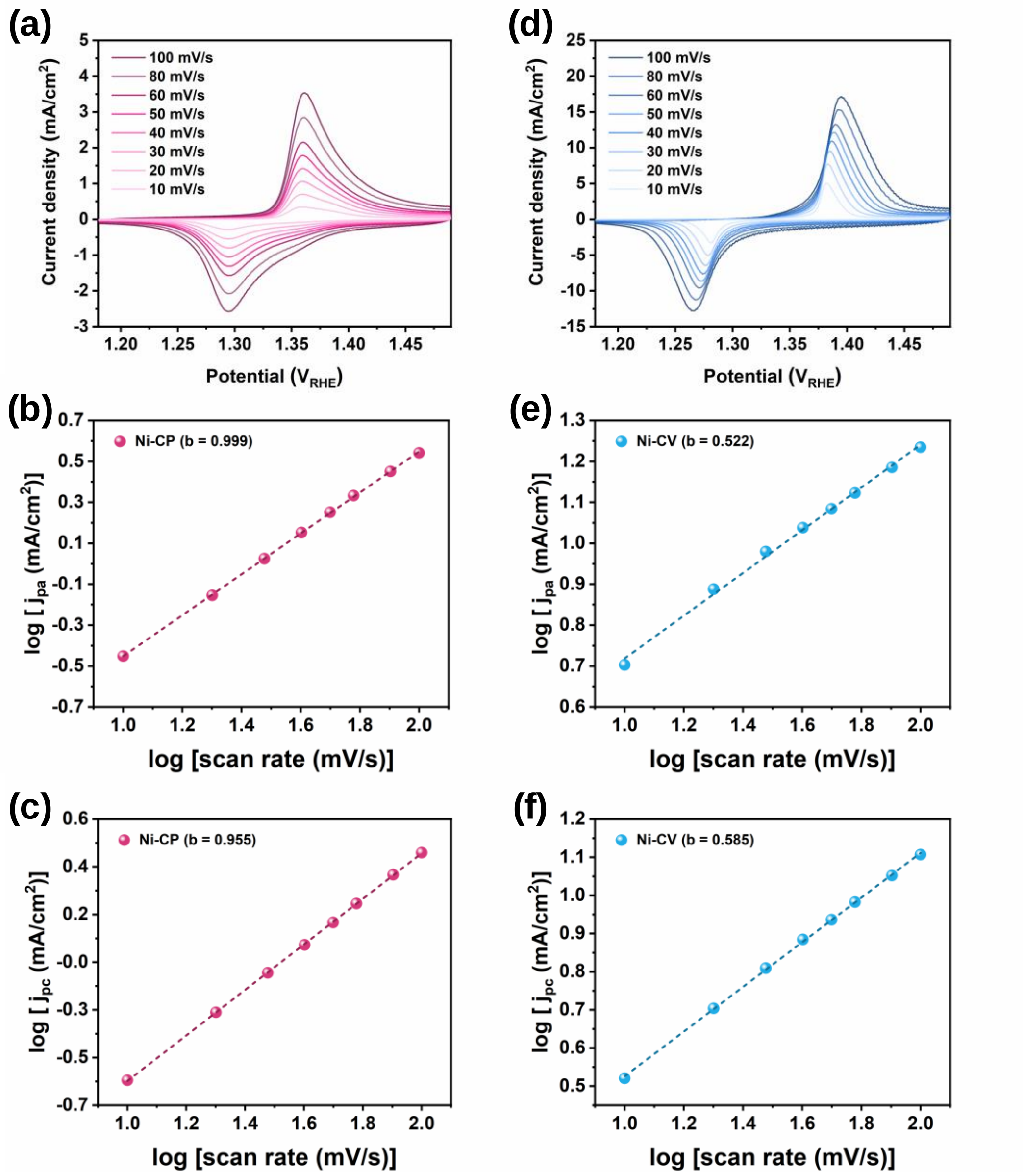

Figure S7. CV analyses of (a-c) Ni-CP and (d-e) Ni-CV at different scan rates in Fe-purified 1 M KOH electrolyte. (a,d) CV curves. Linear plots of (b,e) log [j_{pa}] and (c,f) log [j_{pc}] with respect to log [scan rate]. Here, j_{pa} and j_{pc} represent anodic and cathodic redox peak current density, respectively.

It is assumed that if there is any transport limitation to the redox active Ni sites, which are related to OER active sites, the OER activity is also affected by transport limitation (diffusion limitation).

The scan rate-dependent CV analyses of the Ni redox peaks were conducted for Ni-CP and Ni-CV (**Figure S7a,d**). The redox peak current density and scan rate have a relationship of $j = av^b$, where j is the current density, ν is the scan rate, a and b are adjustable parameters. This relationship can be used to determine whether the kinetics of Ni redox reaction ($Ni^{2+/3+}$) is surface-controlled or diffusion-controlled.[10] When b =1, the redox reaction is surface-controlled (without any diffusion limitation), whereas when b = 0.5, the redox reaction is diffusion-controlled. The b-value can be obtained as the slope of the plot of log [j] vs. log [ν]. **Figure S7b,c,e,f** shows that b-values of Ni-CP from anodic and cathodic redox peaks are close to 1, whereas those of Ni-CV are close to 0.5. This indicates that the redox reaction of Ni-CP with a relatively thin NiO_xH_y layer is surface-controlled while that of Ni-CV with the thicker NiO_xH_y layer is diffusion-controlled. Therefore, it is concluded that there is a significant transport limitation for Ni-CV compared to Ni-CP.

For the interpretation of “diffusion-controlled” phenomena, we believe this “diffusion-controlled” phenomenon is not related to the mass transport limitation of OH^{-}, which is a reactant for both redox reaction and OER. This is because sufficient amounts of OH^- are present in 1 M KOH electrolyte with pH 14 and the OER operating current density (a few mA/cm^2) is too low to cause mass transport limitation of OH^- in pH 14. This interpretation is also consistent with the RDE experiment of the 300-NiSe/RDE-CV sample in the following part of this paper that shows no OER activity difference between with and without rotation (**Figure S19b).**

Instead. this diffusion-controlled phenomena for the Ni redox sites of Ni-CV can be rather explained by diffusion-controlled charge transport (or charge percolation) *via* proton-coupled electron hopping through the hydrous NiO_xH_y layer. The electrochemical conditioning of Ni-based materials (*e.g.*, Ni, NiO, NiSe, etc.) forms a microdispersed hydrated oxide structure with a chemical formula of $[Ni_2(OH)_6(OH_2)_3]^{2-}$ on the surface (in contact with electrolyte) or even in the bulk (underneath the surface).[11–13] This hydrated oxide layer has amorphous nature, varying composition depending on the degree of water coordination, and mixed electron-proton conductivity. The redox reaction of $Ni(OH)_2$/NiOOH and oxygen evolution reaction (OER), which involve proton transfer together with electron transfer, occur *via* proton-coupled electron transfer.[14] Additionally, in such system, the transport of electrons through hydrated oxide film can be coupled with the transfer of protons, which is termed proton-electron hopping.[15] In this regard, it is understood that for Ni-CV with a relatively thick NiO_xH_y layer, the charge is propagated *via* self-exchange proton-electron hopping between homogeneously distributed set of redox active sites in the hydrated NiO_xH_y layer, which is diffusion-controlled. On the other hand, as to Ni-CP with a thin NiO_xH_y layer, since the Ni redox sites are adjacent to the support electrode (*i.e.*, Ni metal), their redox reaction is dominantly affected by the electrode potential, showing the surface-controlled characteristics.[11,12,15] Similar scan-rate dependency of redox peaks was also observed for thin (surface-controlled) and thick (diffusion-controlled) hydrous Fe oxide film.[16] Thus, it is concluded that Ni-CV suffers from diffusion limitation for charge transport, not for mass transport of OH^-.

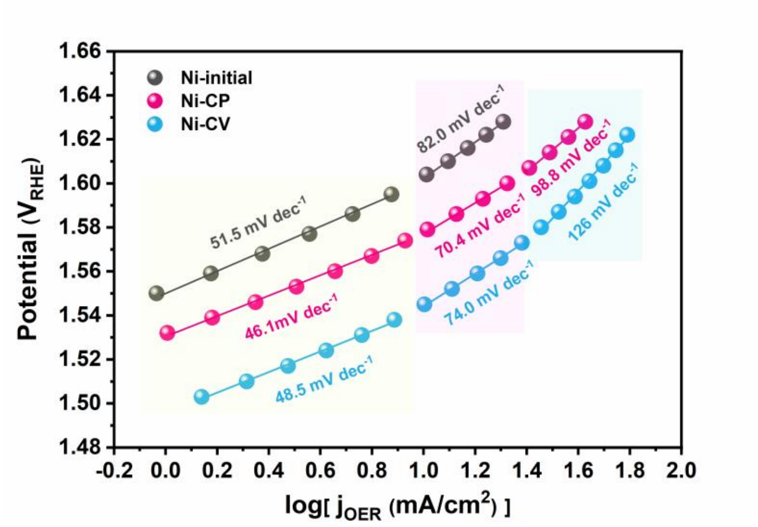

Figure S8. Tafel slopes of Ni-initial, Ni-CP, and Ni-CV in Fe-unpurified 1 M KOH.

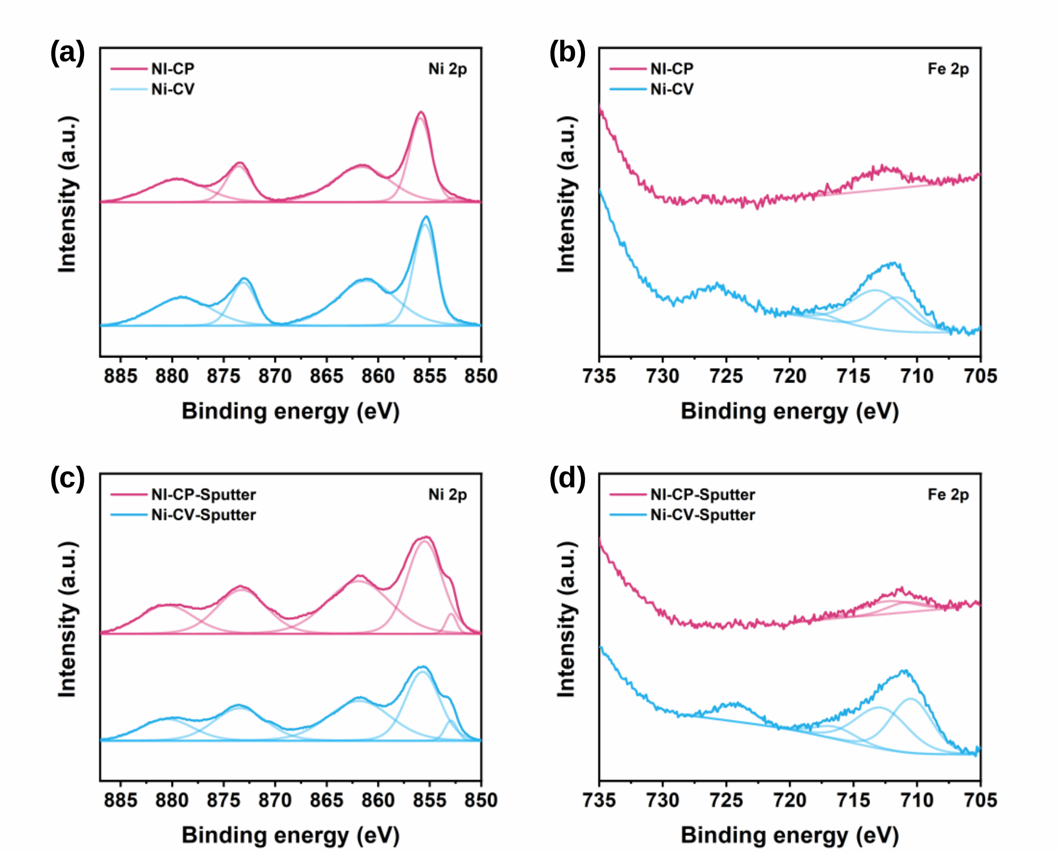

Figure S9. XPS spectra of Ni foil after CP and CV electrochemical conditioning in Fe-unpurified 1 M KOH electrolyte. (a) Ni 2p and (b) Fe 2p before Ar$^+$ sputter. (c) Ni 2p and (d) Fe 2p after Ar$^+$ sputter.

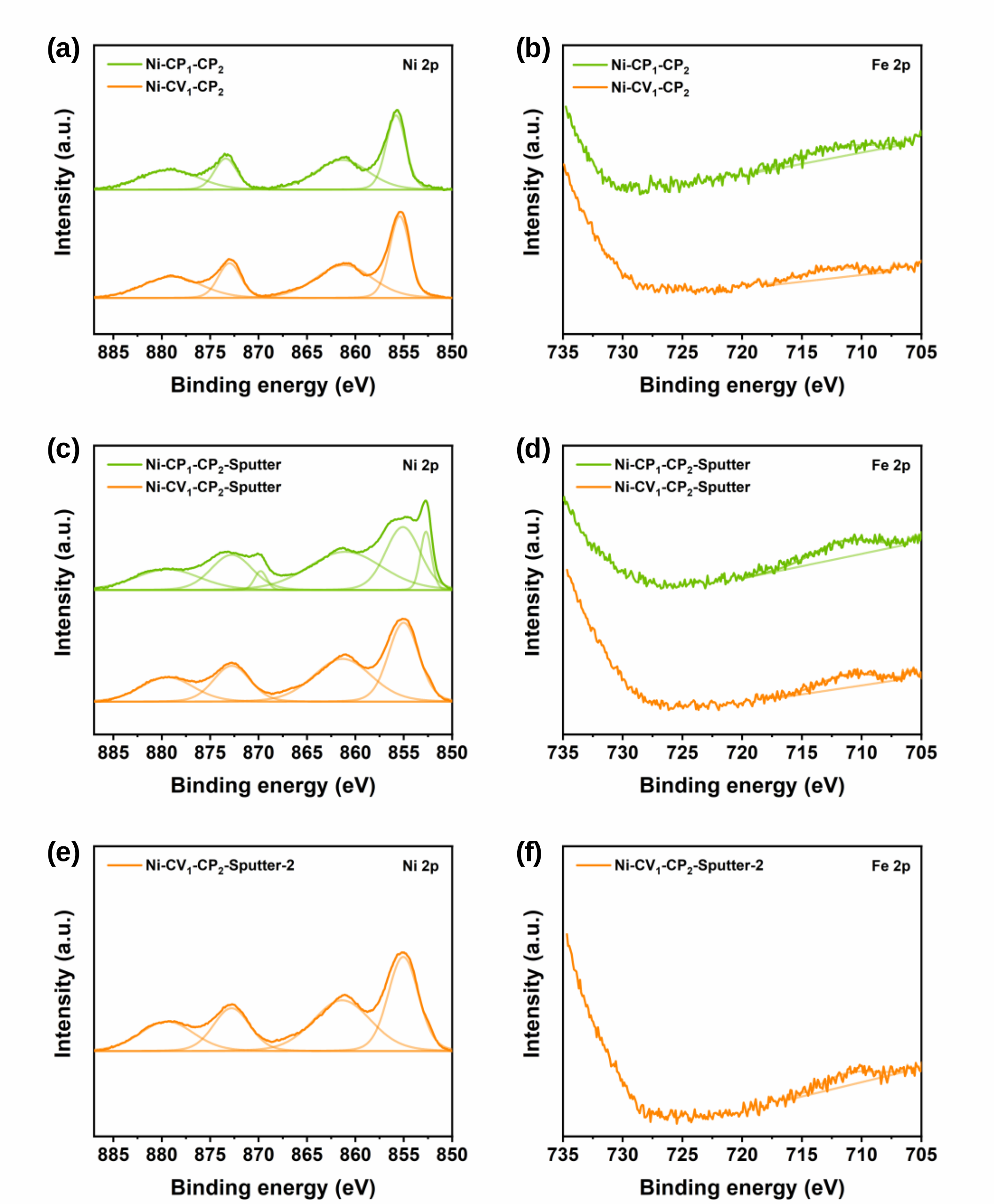

Figure S10. XPS spectra of Ni-CP_1-CP_2 and Ni-CV_1-CP_2. (a) Ni 2p and (b) Fe 2p before Ar^+ sputter. (c) Ni 2p and (d) Fe 2p after Ar^+ sputter. (e) Ni 2p and (f) Fe 2p after further Ar^+ sputter for Ni-CV_1-CP_2.

Table S3. XPS data of Ni-CP, Ni-CV in Fe-unpurified 1 M KOH electrolyte and Ni-CP_1-CP_2 and Ni-CV_1-CP_2. (Relative sensitivity factors for Ni $2p_{3/2}$ and Fe $2p_{3/2}$ are 2.563 and 1.965, respectively).

	Area		RSF-corrected		Composition (%)	
	Ni $2p_{3/2}$	Fe $2p_{3/2}$	Ni $2p_{3/2}$	Fe $2p_{3/2}$	Ni	Fe
Ni-CP	115621	4979	45106	2534	94.7	5.3
Ni-CV	145122	17268	56614	8789	86.6	13.4
Ni-CP_1-CP_2	27618	1248	10774	635	94.4	5.6
Ni-CV_1-CP_2	76901	1930	30000	982	96.7	3.3
Ni-CP-Sputter	310872	6517	121277	3317	97.3	2.7
Ni-CV-Sputter	224781	29204	87691	14865	85.5	14.5
Ni-CP_1-CP_2-Sputter	120773	2734	47116	1391	97.1	2.9
Ni-CV_1-CP_2-Sputter	123600	2027	48218	1032	97.9	2.1
Ni-CV_1-CP_2-Sputter-2	119781	1275	46728	649	98.6	1.4

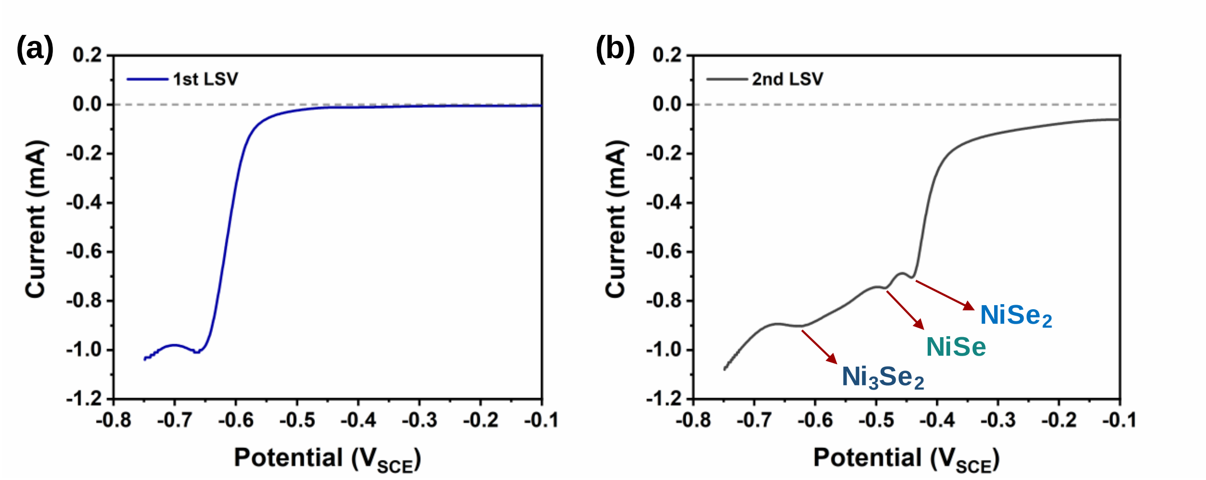

Figure S11. Linear sweep voltammetry (LSV) curve of the FTO glass substrate in the electrolyte containing $NiCl_2$, SeO_2, and LiCl for the electrodeposition of NiSe film at a scan rate of 10 mV/s without stirring by a magnetic bar. (a) 1st LSV. (b) 2nd LSV. In panel b, the interpretation of redox peak for each NiSe crystal phase refers to the previous report.[17]

Electrodeposition of nickel selenide on fluorine-doped tin oxide (FTO) glass and Ni foil substrates was conducted in the electrodeposition bath containing 65 mM $NiCl_2$, 10 mM SeO_2, and 100 mM LiCl. The electrodeposition condition was optimized to grow uniform, compact, and single-phase nickel selenide film. When electrodeposition via a chronoamperometry (CA) was tried on FTO glass substrate at potentials in the range of -0.35 to -0.6 V_{SCE} according to the previous report,[17] there occurred two issues. Firstly, red particles, which are suspected to be amorphous Se given that Se is produced as a reaction intermediate for electrodeposition of NiSe and amorphous Se has a red color, were grown on the FTO glass substrate instead of nickel selenide, Secondly, red particles started to form islands as electrodeposition time increased, instead of growing uniform and thick film. The first issue of growing red particles can be related to the wrong choice of potential range for electrodeposition of nickel selenide. The second issue of non-uniform island formation during electrodeposition can be related to the lack of uniform nucleation sites on the FTO glass substrate. To figure out the reasons for these two issues, linear sweep voltammetry (LSV) analysis was conducted.

After one sweep of LSV in the potential range of -0.1 to -0.75 V_{SCE}, it was observed that thin and uniform black (or gray) film was grown on the FTO glass substrate. After the subsequent

2nd sweep of LSV, black (or gray) film became darker while maintaining the uniformity without forming islands. These LSV results imply the possibility of solving the second issue (mentioned in the previous paragraph) of non-uniform island formation during electrodeposition by conducting LSV pretreatment before electrodeposition via CA. However, it was found that characteristics of LSV curve (e.g., number of redox peaks and redox peak potentials) changed dramatically from the 1st to the 2nd sweep of LSV (**Figure S11**). It is suspected that the reason for the evolution of LSV characteristics after 1st LSV sweep is the enhanced affinity of electrodeposition electrolyte for the substrate after deposition of initial nickel selenide layer on FTO glass during the 1st LSV sweep compared to that for pure FTO glass surface.

Among various phases of nickel selenides, such as $NiSe_2$, Ni_3Se_4, Ni_6Se_5, NiSe, Ni_3Se_2, and $Ni_{0.85}Se$, it has been reported that three phases of nickel selenides including $NiSe_2$, NiSe, and Ni_3Se_2 can be synthesized via electrodeposition by changing the deposition potential.[17,18] During the electrodeposition of nickel selenides, the following (electro)chemical reactions can occur depending on the deposition potential.[17]

$$SeO_2 + H_2O \leftrightarrow H_2SeO_3 \tag{1}$$

$$H_2SeO_3 + 4H^+ + 4e^- \leftrightarrow Se + 3H_2O \tag{2}$$

$$Se + 2H^+ + 2e^- \leftrightarrow H_2Se \tag{3}$$

$$H_2Se + Ni^{2+} \leftrightarrow NiSe + 2H^+ \tag{4}$$

$$H_2Se + Se + Ni^{2+} \leftrightarrow NiSe_2 + 2H^+ \tag{5}$$

$$2NiSe + Ni^{2+} + 2e^- \leftrightarrow Ni_3Se_2 \tag{6}$$

Also, three redox peaks in **Figure S11b** can be assigned as electrochemical reactions for the synthesis of $NiSe_2$, NiSe, and Ni_3Se_2 in the order of increasing potential in the negative direction, respectively.[17] Based on the understanding of each redox peak, we aimed to grow uniform and single-phase NiSe film using CA at -0.5 V_{SCE}, which is right after the redox peak potential for NiSe synthesis. For this, one sweep of LSV pretreatment without stirring was first conducted in the potential range of -0.1 to -0.75 V_{SCE} to grow the initial nucleation layer and then, subsequent CA at -0.5 V_{SCE} with stirring was carried out for different electrodeposition times (300, 600, and 900 s). Unfortunately, although red particles synthesis can be avoided in this way, SEM images in **Figure S12** show that the grown nickel selenide films with different electrodeposition times have distinct and non-uniform particle sizes and shapes. The electrodeposition condition was further optimized to grow uniform single-phase NiSe film with varying electrodeposition times. It was found that the optimized electrodeposition condition is one sweep of LSV pretreatment in the potential range of -0.1 to -0.75 V_{SCE} without stirring, and then subsequent CA at -0.51 V_{SCE} with stirring. The SEM and EDX mapping images of NiSe film on FTO glass electrodeposited using the optimized condition in **Figure S13** indicate that NiSe films were uniformly grown in terms of particle size and shape as well as chemical compositions.

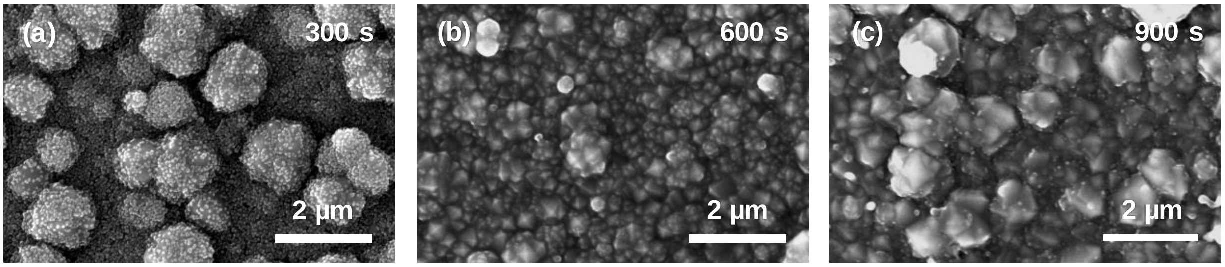

Figure S12. SEM images of nickel selenide films grown on the FTO glass via electrodeposition employing 1st LSV pretreatment and then a chronoamperometry (CA) at -0.50 V_{SCE} for (a) 300 s, (b) 600 s, and (c) 900 s.

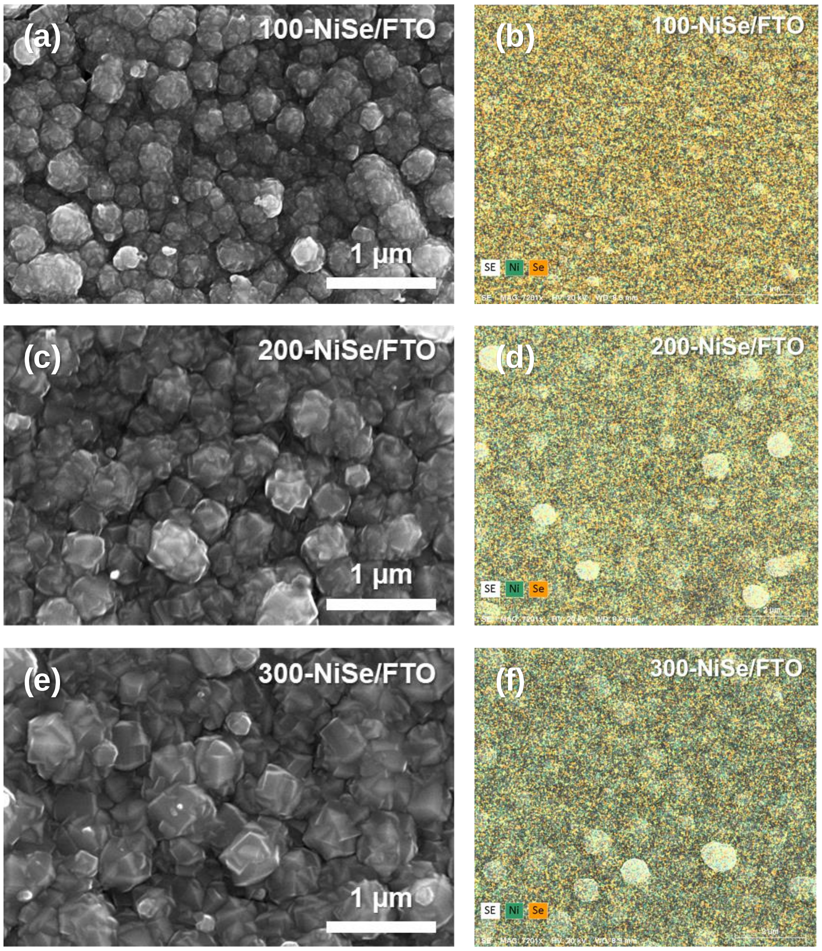

Figure S13. SEM and EDX mapping images of NiSe films grown on the FTO glass via electrodeposition employing 1st LSV pretreatment and then a CA at -0.51 V_{SCE} for (a,b) 100 s, (c,d) 200 s, and (e,f) 300 s.

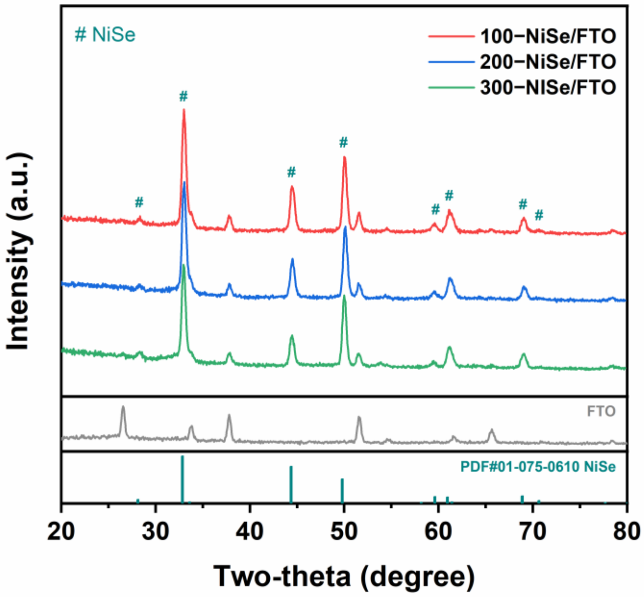

Figure S14. GIXRD spectra of x-NiSe/FTO.

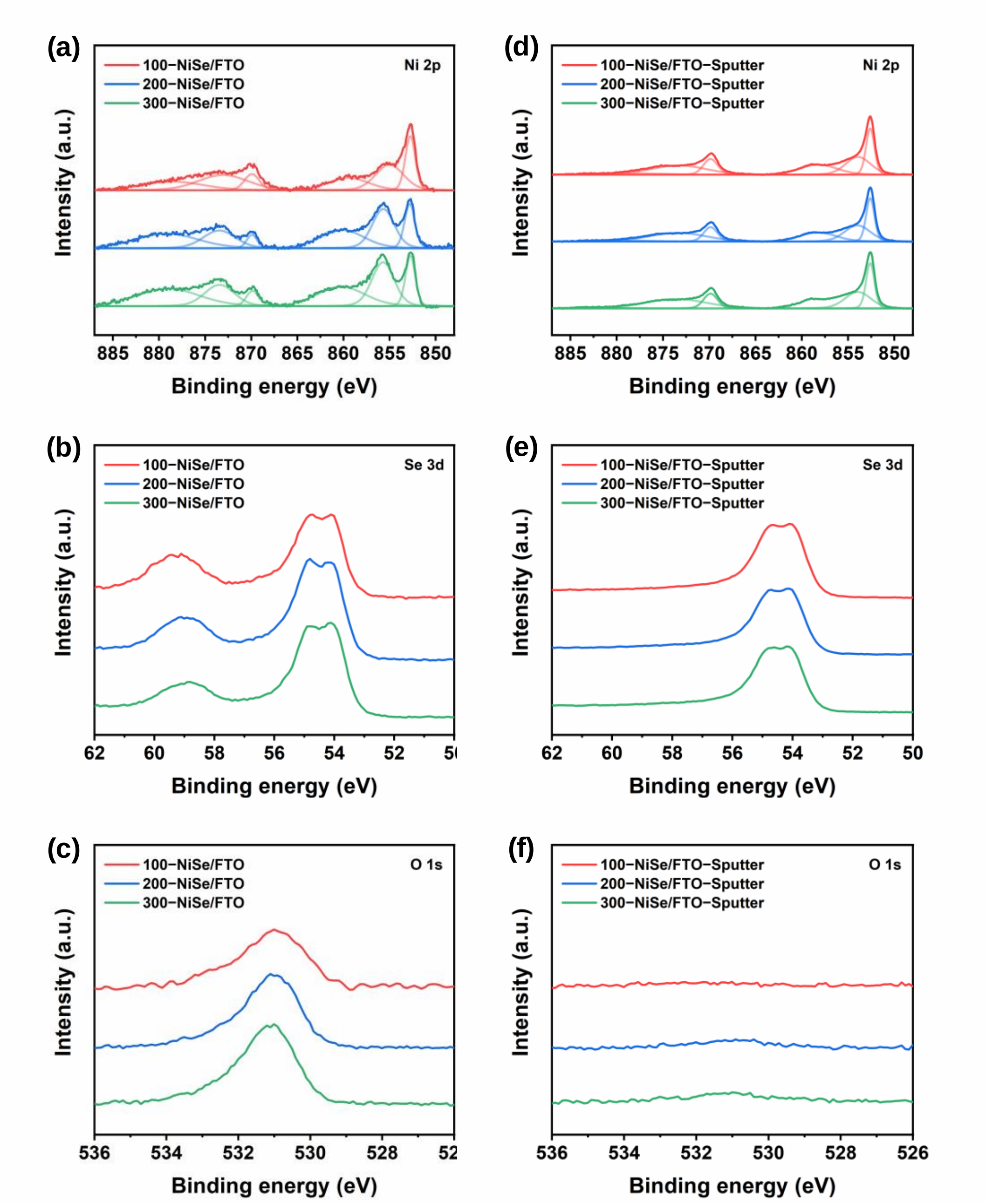

Figure S15. XPS spectra of x-NiSe/FTO. (a) Ni 2p, (b) Se 3d, and (c) O 1s before Ar$^+$ sputter. (d) Ni 2p, (e) Se 3d, and (f) O 1s after Ar$^+$ sputter.

The chemical composition and state of x-NiSe/FTO were analyzed by XPS on the surface and in the bulk employing Ar$^+$ sputtering (**Figure S15**). Here, x-NiSe/FTO samples after Ar$^+$ sputtering were denoted as x-NiSe/FTO-Sputter. All the x-NiSe/FTO showed almost identical XPS spectra in the Ni 2p, Se 3d, and O 1s regions, indicating their identical chemical composition and state. As to XPS analyses on the surface, x-NiSe/FTO had Ni $2p_{3/2}$ peaks at binding energies of 852.8 eV assigned to Ni^{2+} from NiSe and at 855.6 eV assigned to NiO_xH_y (**Figure S15a**).[18–21] The Se 3d spectra showed the peaks at 54.1 and 54.9 eV that belong to the $3d_{5/2}$ and $3d_{3/2}$ spectra of Se^{2-} from NiSe. The peak at around 59.0 eV is attributed to the SeO_x (**Figure S15b**).[18,20,21] The O 1s spectra exhibited a peak at around 531.1 eV, which matches the presence of the oxidized species on the surface such as NiO_xH_y and SeO_x (**Figure S15c**). As to XPS analyses of the bulk, x-NiSe/FTO-Sputter had Ni $2p_{3/2}$ peaks at 852.8 and 853.9 eV that are attributed to Ni^{2+} and Ni^{3+} from NiSe,[18] while the Ni $2p_{3/2}$ peak for NiO_xH_y at 855.6 eV was not observed (**Figure S15d**). The Se 3d peaks for NiSe at 54.1 and 54.9 eV existed in the bulk, but the peak for SeO_x at around 59.0 eV disappeared (**Figure S15e**). As to the O 1s spectra, x-NiSe/FTO-Sputter did not exhibit a noticeable O 1s signal (**Figure S15f**). Collectively, these surface and bulk XPS analysis results for x-NiSe/FTO suggest that only pure NiSe was successfully grown during electrodeposition and the oxidized species on the surface such as NiO_xH_y and SeO_x were formed after electrodeposition by surface oxidation of NiSe possibly due to resting in aqueous electrodeposition solution, rinsing with deionized water, or exposure to air after electrodeposition.

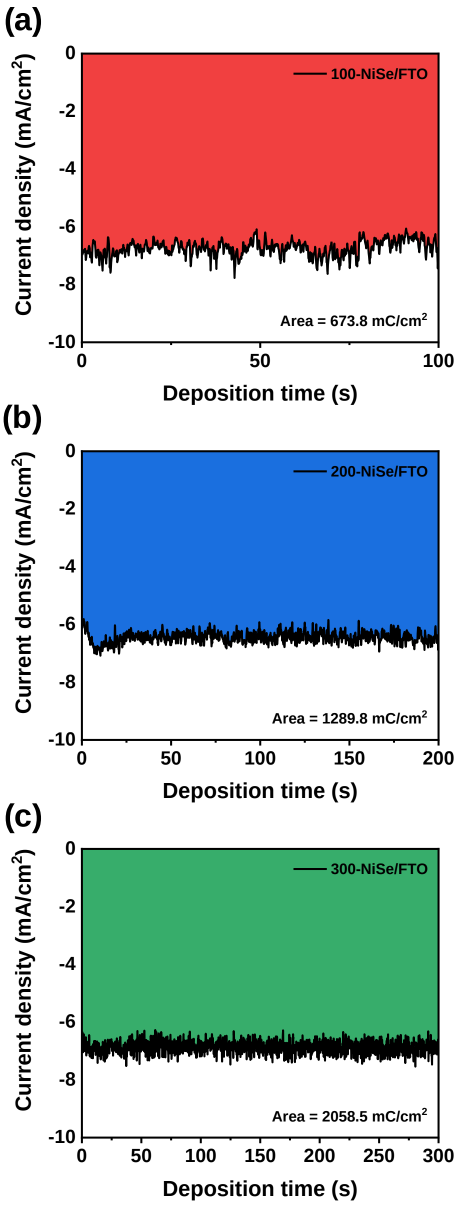

Figure S16. Electrodeposition of NiSe film on the FTO glass substrate employing CA at -0.51 V_{SCE} with different deposition times of (a) 100 s, (b) 200 s, and (c) 300 s. The colored area represents the faradaic charge that was passed during the electrodeposition of NiSe.

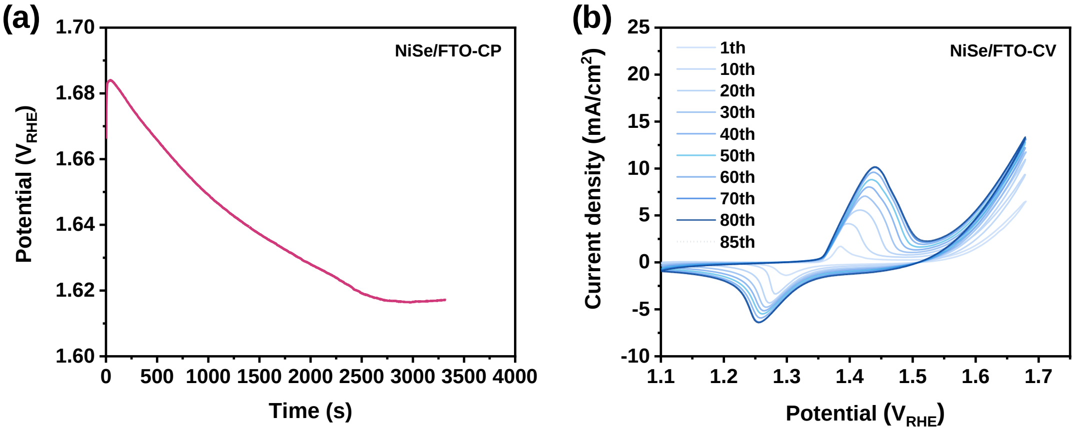

Figure S17. Electrochemical conditioning of NiSe/FTO using (a) CP at 5 mA/cm^2 and (b) CV at a scan rate of 10 mV/s in Fe-purified 1 M KOH electrolyte.

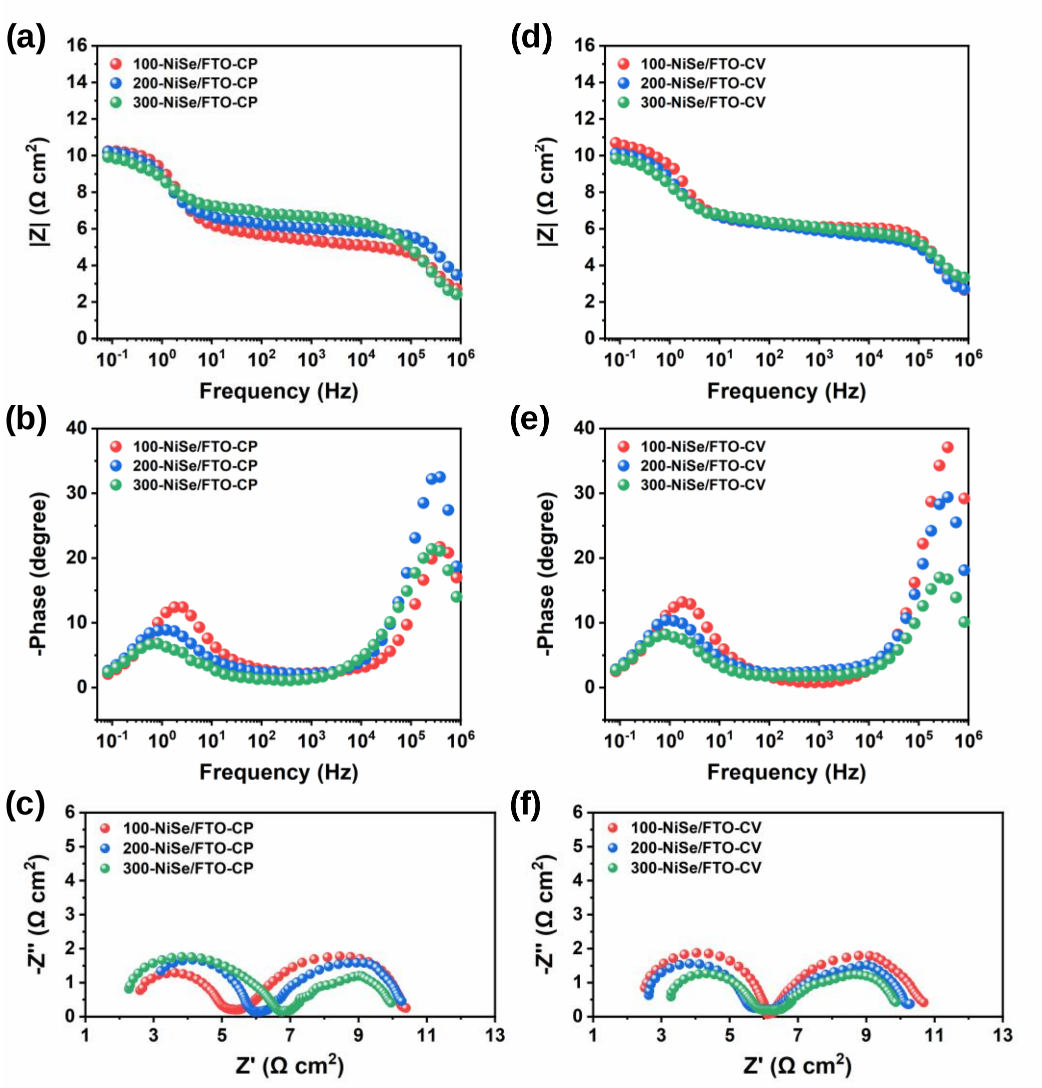

Figure S18. EIS spectra of (a-c) x-NiSe/FTO-CP and (d-f) x-NiSe/FTO-CV measured at 1.68 V_{RHE} in Fe-purified 1 M KOH electrolyte. (a,b,d,e) Bode plots, (c,f) Nyquist plots.

Table S4. Electrochemical parameters obtained by fitting the EIS data of x-NiSe/FTO-CP and x-NiSe/FTO-CV at 1.68 V_{RHE} in Fe-purified 1 M KOH electrolyte. Measurements were taken at least three times and average values are presented with the standard error bar.

	R_t [Ω cm^2]	R_{ct} [Ω cm^2]	C_{dl} [mF/cm^2]
100-NiSe/FTO-CP	3.4 ± 0.7	3.7 ± 0.4	34.2 ± 2.2
200-NiSe/FTO-CP	3.6 ± 0.1	2.9 ± 0.2	80.8 ± 13.0
300-NiSe/FTO-CP	3.3 ± 0.2	2.5 ± 0.2	112.5 ± 11.5
100-NiSe/FTO-CV	2.5 ± 0.9	4.1 ± 1.0	34.5 ± 7.4
200-NiSe/FTO-CV	4.8 ± 0.6	3.0 ± 0.1	86.9 ± 9.7
300-NiSe/FTO-CV	4.9 ± 0.2	2.3 ± 0.3	136.7 ± 13.0

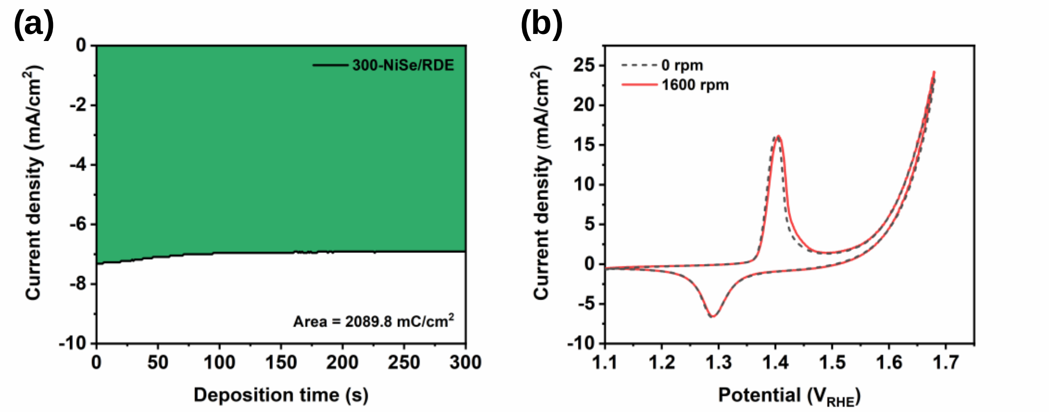

Figure S19. (a) Electrodeposition of NiSe film on the RDE for 300 s employing CA at -0.51 V_{SCE}. (b) CV curves of 300-NiSe/RDE-CV at 10 mV/s with 0 rpm and 1600 rpm in Fe-purified 1 M KOH electrolyte. It is noted that any remaining O_2 bubble for the 0 rpm sample was removed before the OER onset to fairly observe the effect of reactant OH^- mass transport on the OER activity.

To confirm whether there is any mass transport limitation through the NiSe-derived NiO_xH_y layer, OER testing using rotation disk electrode (RDE) was applied to NiSe film. NiSe film was electrodeposited on RDE for 300 s by using the same electrodeposition condition as for 300-NiSe/FTO sample, and was denoted as 300-NiSe/RDE (**Figure S19a**). Here, 300-NiSe sample was chosen since this would suffer the most severe mass transport limitation among x-NiSe samples due to its thickest layer. In **Figure S19b**, the OER activity of 300-NiSe/RDE without any rotation (0 rpm) and with rotation at 1600 rpm was identical. One might suspect that the convection by RDE only affects the diffusion layer above the external surface area of NiSe-derived NiO_xH_y layer, not the inner surface area within NiSe-derived porous NiO_xH_y layer effectively depending on its pore size and hydrophilicity. Nevertheless, we believe there is no mass transport limitation of reactant OH^- for OER in this study given that for 1 M KOH electrolyte with pH 14, sufficient amounts of OH^- are present even in the electrolyte within the NiSe-derived porous NiO_xH_y layer as well as OER operating current density (a few tens of mA/cm^2) is too low to cause mass transport limitation of OH^- in pH 14. Also, this OER activity independent of rotating speed implies that there is no mass transport limitation of O_2 bubble products apparently for 300-NiSe sample.[22] Therefore, the asymmetrical shapes of EIS Nyquist plots of x-NiSe/FTO samples in **Figure S18c,f** are attributed to electron transport resistance, not mass transport resistance of OH^- reactant.

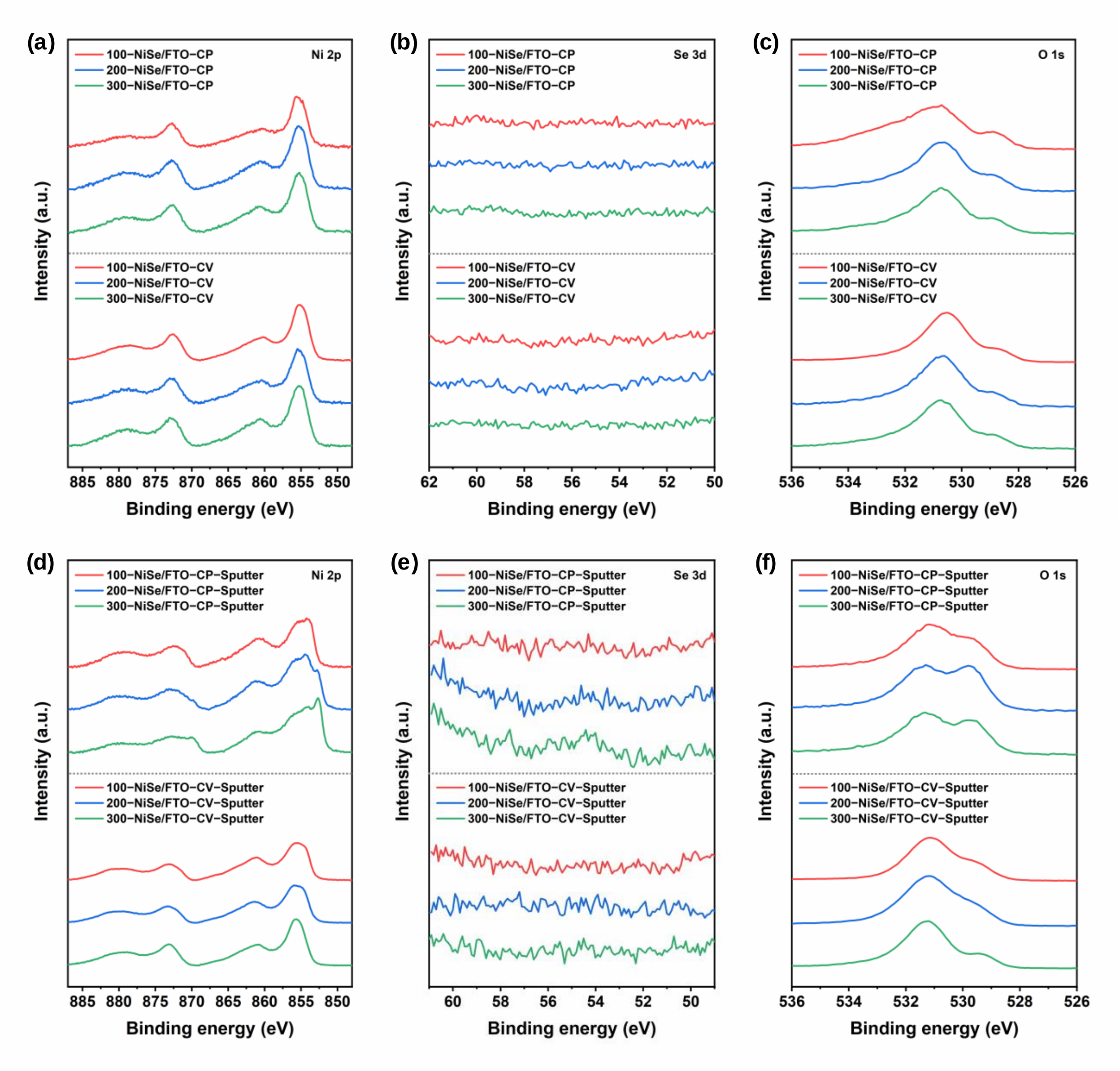

Figure S20. XPS spectra of x-NiSe/FTO-CP and x-NiSe/FTO-CV. (a) Ni 2p, (b) Se 3d, and (c) O 1s before Ar^+ sputter. (d) Ni 2p, (e) Se 3d, and (f) O 1s after Ar^+ sputter.

As to XPS analyses on the surface, all the x-NiSe/FTO-CP and x-NiSe/FTO-CV exhibited almost identical XPS spectra for Ni 2p, Se 3d, and O 1s regions (**Figure S20a−c**). Only the Ni $2p_{3/2}$ peak corresponding to NiO_xH_y at 855.6 eV was observed, and all the Se 3d peaks disappeared. These observations suggest that NiSe material on the surface of all the x-NiSe/FTO samples was completely *in situ* oxidized and transformed into NiO_xH_y during CP and CV electrochemical conditioning, and Se from NiSe was leached into the electrolyte. Unlike XPS analyses on the surface, x-NiSe/FTO-CP and x-NiSe/FTO-CV showed a difference in the bulk (**Figure S20d−f**). Here, x-NiSe/FTO-CP and x-NiSe/FTO-CV after Ar^+ sputtering were denoted as x-NiSe/FTO-CP-Sputter and x-NiSe/FTO-CV-Sputter, respectively. As for Ni $2p_{3/2}$ peaks, all the x-NiSe/FTO-CV-Sputter only exhibited a peak at 855.6 eV assigned to NiO_xH_y. On the other hand, x-NiSe/FTO-CP-Sputter showed peaks at 855.6 eV for NiO_xH_y and at 853.9 eV, which can be assigned to Ni^{3+} from NiSe or Ni^{2+} from NiO.[18,19] Furthermore, 200- and 300-NiSe/FTO-CP-Sputter exhibited the additional peak at 852.8 eV that is associated with NiSe,[18,20,21] and its relative intensity became greater for 300-NiSe/FTO-CP-Sputter compared to 200-NiSe/FTO-CP-Sputter. As for Se 3d spectra, while x-NiSe/FTO-CV-Sputter and 100-NiSe/FTO-CP-Sputter did not exhibit any noticeable peak, 200- and 300-NiSe/FTO-CP-Sputter exhibited a weak but discernible Se 3d peak. Moreover, the Se 3d signal for 300-NiSe/FTO-CP-Sputter was slightly greater than that of 200-NiSe/FTO-CP-Sputter. Also, O 1s spectra, while not observed for x-NiSe/FTO-Sputter before electrochemical conditioning, were observed for all the x-NiSe/FTO-CP-Sputter and x-NiSe/FTO-CV-Sputter samples. Based on Ni 2p, Se 3d, and O 1s spectra in the bulk, it is concluded that *in situ* oxidation occurred throughout the entire NiSe layer for all the x-NiSe/FTO-CP and x-NiSe/FTO-CV. However, while x-NiSe/FTO-CV and 100-NiSe/FTO-CP underwent complete *in situ* oxidation, 200- and 300-NiSe/FTO-CP underwent partial *in situ* oxidation, leaving the NiSe and NiO_xH_y together within the bulk NiSe layer. Moreover, it was found that 300-NiSe/FTO-CP with a thicker NiSe layer maintained more NiSe than 200-NiSe/FTO-CP.

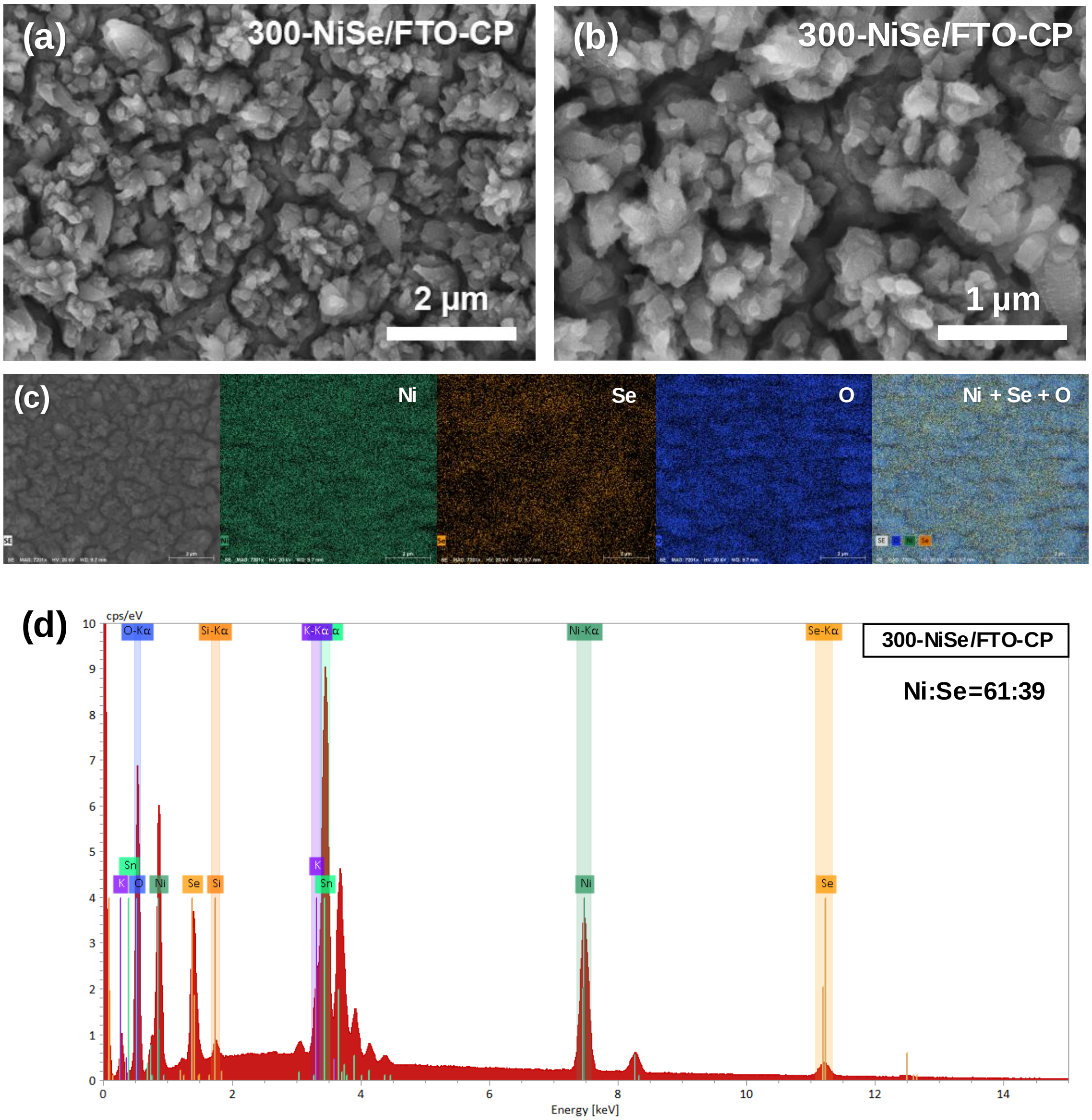

Figure S21. SEM and EDX analyses of 300-NiSe/FTO-CP. (a,b) SEM images. (c) EDX mapping images of Ni, Se, and O. (d) EDX spectrum.

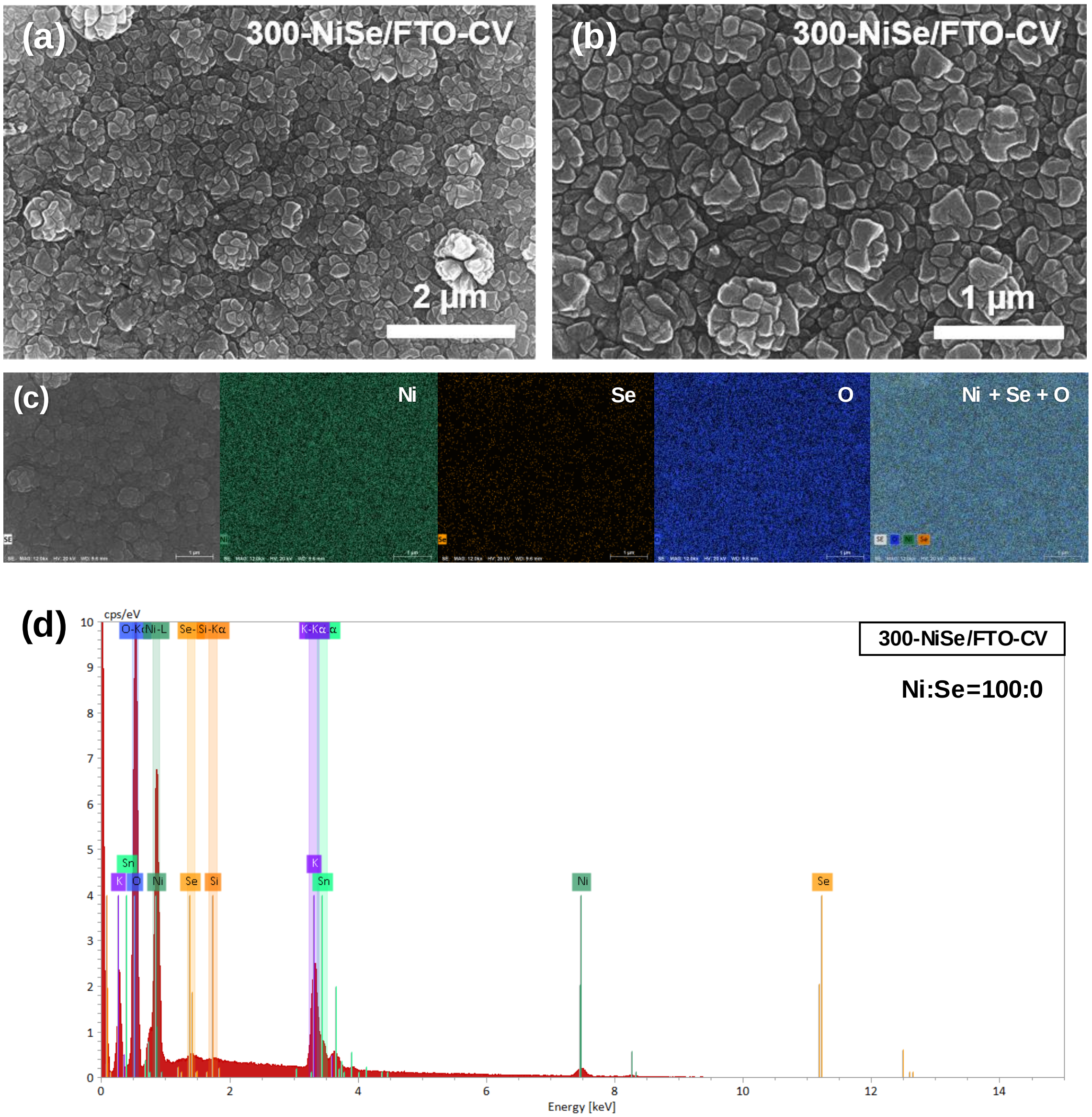

Figure S22. SEM and EDX analyses of 300-NiSe/FTO-CV. (a,b) SEM images. (c) EDX mapping images of Ni, Se, and O. (d) EDX spectrum.

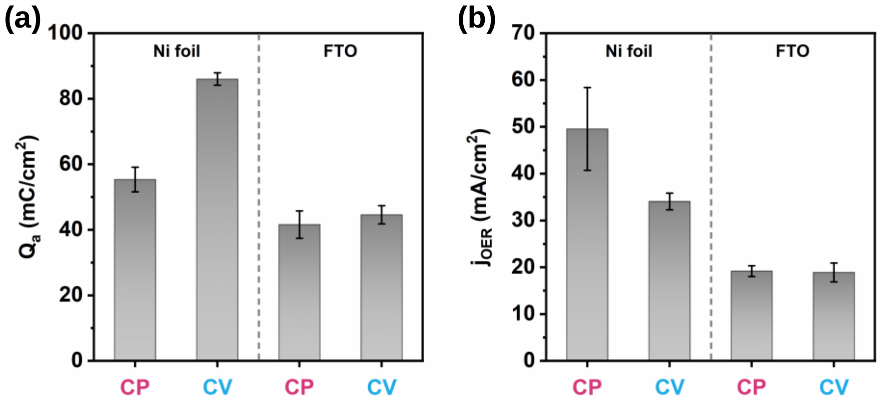

Figure S23. The comparison of (a) Q_a and (b) j_{OER} of 100-NiSe/Ni-CP, 100-NiSe/Ni-CV, 100-NiSe/FTO-CP, and 100-NiSe/FTO-CV.

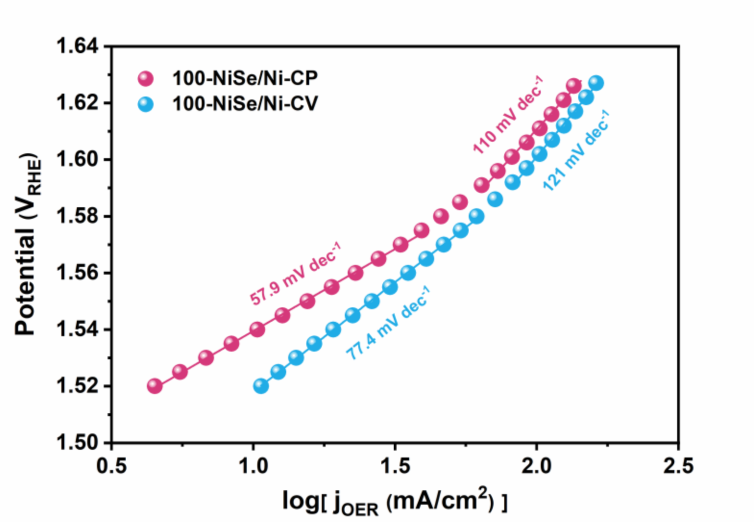

Figure S24. Tafel slopes of 100-NiSe/Ni-CP and 100-NiSe/Ni-CV in Fe-unpurified 1 M KOH.

Table S5. XPS data of 100-NiSe/Ni after CP and CV electrochemical conditioning in Fe-unpurified 1 M KOH electrolyte on several different positions (Relative sensitivity factors for Ni $2p_{3/2}$ and Fe $2p_{3/2}$ are 2.563 and 1.965, respectively)

	Area		RSF-corrected		Composition (%)	
	Ni $2p_{3/2}$	Fe $2p_{3/2}$	Ni $2p_{3/2}$	Fe $2p_{3/2}$	Ni	Fe
100-NiSe/Ni-CP-Sputter 1	117587	14753	45873	7509	88.4 ± 1.3	11.6 ± 1.3
100-NiSe/Ni-CP-Sputter 2	155790	15002	60776	7636		
100-NiSe/Ni-CP-Sputter 3	170730	13853	66605	7051		
100-NiSe/Ni-CV-Sputter 1	20533	3010	8010	1532	83.6 ± 0.3	16.4 ± 0.3
100-NiSe/Ni-CV-Sputter 2	34692	5367	13534	2732		

REFERENCES

(1) Chung, D. Y.; Lopes, P. P.; Farinazzo Bergamo Dias Martins, P.; He, H.; Kawaguchi, T.; Zapol, P.; You, H.; Tripkovic, D.; Strmcnik, D.; Zhu, Y.; Seifert, S.; Lee, S.; Stamenkovic, V. R.; Markovic, N. M. Dynamic Stability of Active Sites in Hydr(Oxy)Oxides for the Oxygen Evolution Reaction. *Nat. Energy* **2020**, *5*, 222–230.

(2) Vrubel, H.; Moehl, T.; Grätzel, M.; Hu, X. Revealing and Accelerating Slow Electron Transport in Amorphous Molybdenum Sulphide Particles for Hydrogen Evolution Reaction. *Chem. Commun.* **2013**, *49*, 8985–8987.

(3) Bisquert, J. Theory of the Impedance of Electron Diffusion and Recombination in a Thin Layer. *J. Phys. Chem. B* **2002**, *106*, 325–333.

(4) Song, L.; Zhao, M.; Li, X.; Zhang, Z.; Qu, L. Solution-Processed MoS_2 Nanotubes/Reduced Graphene Oxide Nanocomposite as an Active Electrocatalyst toward the Hydrogen Evolution Reaction. *RSC Adv.* **2016**, *6*, 70740–70746.

(5) Trotochaud, L.; Young, S. L.; Ranney, J. K.; Boettcher, S. W. Nickel–Iron Oxyhydroxide Oxygen-Evolution Electrocatalysts: The Role of Intentional and Incidental Iron Incorporation. *J. Am. Chem. Soc.* **2014**, *136*, 6744–6753.

(6) Wehrens-Dijksma, M.; Notten, P. H. L. Electrochemical Quartz Microbalance Characterization of Ni(OH)2-Based Thin Film Electrodes. *Electrochimica Acta* **2006**, *51*, 3609–3621.

(7) Hall, D. S.; Lockwood, D. J.; Poirier, S.; Bock, C.; MacDougall, B. R. Applications of in Situ Raman Spectroscopy for Identifying Nickel Hydroxide Materials and Surface Layers during Chemical Aging. *ACS Appl. Mater. Interfaces* **2014**, *6*, 3141–3149.

(8) Klaus, S.; Cai, Y.; Louie, M. W.; Trotochaud, L.; Bell, A. T. Effects of Fe Electrolyte Impurities on $Ni(OH)_2$ /NiOOH Structure and Oxygen Evolution Activity. *J. Phys. Chem. C* **2015**, *119*, 7243–7254.

(9) Hall, D. S.; Lockwood, D. J.; Poirier, S.; Bock, C.; MacDougall, B. R. Raman and Infrared Spectroscopy of α and β Phases of Thin Nickel Hydroxide Films Electrochemically Formed on Nickel. *J. Phys. Chem. A* **2012**, *116*, 6771–6784.

(10) Fleischmann, S.; Mitchell, J. B.; Wang, R.; Zhan, C.; Jiang, D.; Presser, V.; Augustyn, V. Pseudocapacitance: From Fundamental Understanding to High Power Energy Storage Materials. *Chem. Rev.* **2020**, *120*, 6738–6782.

(11) Lyons, M. E. G.; Cakara, A.; O'Brien, P.; Godwin, I.; Doyle, R. L. Redox, PH Sensing and Electrolytic Water Splitting Properties of Electrochemically Generated Nickel Hydroxide Thin Films in Aqueous Alkaline Solution. *Int J Electrochem Sci* **2012**, *7*, 11768–11795.

(12) Lyons, M. E. G.; Russell, L.; O'Brien, M.; Doyle, R. L.; Godwin, I.; Brandon, M. P. Redox Switching and Oxygen Evolution at Hydrous Oxyhydroxide Modified Nickel Electrodes in Aqueous Alkaline Solution: Effect of Hydrous Oxide Thickness and Base Concentration. *Int J Electrochem Sci* **2012**, *7*, 2710–2763.

(13) Doyle, R. L.; Godwin, I. J.; Brandon, M. P.; Lyons, M. E. G. Redox and Electrochemical Water Splitting Catalytic Properties of Hydrated Metal Oxide Modified Electrodes. *Phys. Chem. Chem. Phys.* **2013**, *15*, 13737.

(14) Bediako, D. K.; Surendranath, Y.; Nocera, D. G. Mechanistic Studies of the Oxygen Evolution Reaction Mediated by a Nickel–Borate Thin Film Electrocatalyst. *J. Am. Chem. Soc.* **2013**, *135*, 3662–3674.

(15) Bediako, D. K.; Costentin, C.; Jones, E. C.; Nocera, D. G.; Savéant, J.-M. Proton–Electron Transport and Transfer in Electrocatalytic Films. Application to a Cobalt-Based O_2-Evolution Catalyst. *J. Am. Chem. Soc.* **2013**, *135*, 10492–10502.

(16) Lyons, M. E. G.; Doyle, R. L.; Brandon, M. P. Redox Switching and Oxygen Evolution at Oxidized Metal and Metal Oxide Electrodes: Iron in Base. *Phys. Chem. Chem. Phys.* **2011**, *13*, 21530.

(17) Zhu, J.; Ni, Y. Phase-Controlled Synthesis and the Phase-Dependent HER and OER Performances of Nickel Selenide Nanosheets Prepared by an Electrochemical Deposition Route. *CrystEngComm* **2018**, *20*, 3344–3352.

(18) Zheng, X.; Han, X.; Liu, H.; Chen, J.; Fu, D.; Wang, J.; Zhong, C.; Deng, Y.; Hu, W. Controllable Synthesis of NixSe ($0.5 \leq x \leq 1$) Nanocrystals for Efficient Rechargeable Zinc–Air Batteries and Water Splitting. *ACS Appl. Mater. Interfaces* **2018**, *10*, 13675–13684.

(19) Son, Y. J.; Kawashima, K.; Wygant, B. R.; Lam, C. H.; Burrow, J. N.; Celio, H.; Dolocan, A.; Ekerdt, J. G.; Mullins, C. B. Anodized Nickel Foam for Oxygen Evolution Reaction in Fe-Free and Unpurified Alkaline Electrolytes at High Current Densities. *ACS Nano* **2021**, *15*, 3468–3480.

(20) Shi, Y.; Du, W.; Zhou, W.; Wang, C.; Lu, S.; Lu, S.; Zhang, B. Unveiling the Promotion of Surface-Adsorbed Chalcogenate on the Electrocatalytic Oxygen Evolution Reaction. *Angew. Chem. Int. Ed.* **2020**, *59*, 22470–22474.

(21) Swesi, A. T.; Masud, J.; Nath, M. Nickel Selenide as a High-Efficiency Catalyst for Oxygen Evolution Reaction. *Energy Environ. Sci.* **2016**, *9*, 1771–1782.

(22) Zheng, J.; Yan, Y.; Xu, B. Correcting the Hydrogen Diffusion Limitation in Rotating Disk Electrode Measurements of Hydrogen Evolution Reaction Kinetics. *J. Electrochem. Soc.* **2015**, *162*, F1470–F1481.